

# Preseismic fault creep and elastic wave amplitude precursors scale with lab earthquake magnitude for the continuum of tectonic failure modes

Srisharan Shreedharan<sup>1</sup>, David Chas Bolton<sup>2</sup>, Jacques Rivière<sup>1</sup>, and Chris Marone<sup>1</sup>

<sup>1</sup>Pennsylvania State University

<sup>2</sup>Department of Geosciences, Pennsylvania State University

November 22, 2022

## Abstract

Tectonic faults fail in a continuum of modes from slow earthquakes to elastodynamic rupture. Precursory variations in elastic wavespeed and amplitude, interpreted as indicators of imminent failure, have been observed in limited experimental and natural settings for this spectrum of slip modes. Such variations are thought to arise from microcracking within and around the fault zone. However, the physical mechanisms and connections to fault creep are not well understood. Here, we vary loading stiffness to generate a range of slip modes and measure fault zone properties using elastic waves transmitted through the fault. We find that elastic wave amplitudes show clear changes before failure. The temporal onset of amplitude reduction scales with lab earthquake magnitude and the magnitude of this reduction varies with fault slip. Our data suggest that continuous seismic monitoring in proximity to natural faults could be useful for assessing fault state and seismic hazard potential.

1     **PRESEISMIC FAULT CREEP AND ELASTIC WAVE AMPLITUDE PRECURSORS**  
2             **SCALE WITH LAB EARTHQUAKE MAGNITUDE FOR THE CONTINUUM OF**  
3                     **TECTONIC FAILURE MODES**

4             **Srisharan Shreedharan<sup>1\*</sup>, David Chas Bolton<sup>1</sup>, Jacques Rivière<sup>2</sup>, Chris Marone<sup>1</sup>**

5  
6             <sup>1</sup>Dept. of Geosciences, Pennsylvania State University, University Park, PA 16802 USA

7             <sup>2</sup>Dept. of Engineering Science and Mechanics, Pennsylvania State University, University Park,  
8                                     PA 16802 USA

9  
10                     **\*Corresponding author: srisharan@psu.edu**

11  
12     **Key points:**

- 13             • P-wave amplitudes reduce at the onset of preseismic creep for laboratory earthquakes  
14             • The size and onset of amplitude precursors scales with earthquake size and fault slip rate  
15             • The microphysical mechanisms responsible for these amplitude precursors are similar for  
16             the spectrum of fault slip modes  
17

18 **Abstract:**

19 Tectonic faults fail in a continuum of modes from slow earthquakes to elastodynamic rupture.  
20 Precursory variations in elastic wavespeed and amplitude, interpreted as indicators of imminent  
21 failure, have been observed in limited experimental and natural settings for this spectrum of slip  
22 modes. Such variations are thought to arise from microcracking within and around the fault zone.  
23 However, the physical mechanisms and connections to fault creep are not well understood. Here,  
24 we vary loading stiffness to generate a range of slip modes and measure fault zone properties  
25 using elastic waves transmitted through the fault. We find that elastic wave amplitudes show  
26 clear changes before failure. The temporal onset of amplitude reduction scales with lab  
27 earthquake magnitude and the magnitude of this reduction varies with fault slip. Our data suggest  
28 that continuous seismic monitoring in proximity to natural faults could be useful for assessing  
29 fault state and seismic hazard potential.

30

31 **Plain Language Summary:**

32 Earthquakes in nature can occur slowly, over many days, or rapidly within a few seconds or  
33 minutes. In a few cases geoscientists have observed, in hindsight, ‘precursory’ changes in  
34 seismic velocities, groundwater levels and attenuation that occurred prior to earthquakes. The  
35 ability to robustly identify these signals and accurately attribute them to imminent earthquakes  
36 could have a profound effect on our hazard preparedness, particularly for coastal communities  
37 where tsunami occur. Here, we study lab earthquakes and send acoustic pulses through  
38 laboratory faults. We show that the amplitudes of these pulses decrease systematically before  
39 failure, providing a clear precursor to failure. The magnitude of this lab earthquake precursor is  
40 related to the amount of pre-earthquake fault slip during both slow and fast laboratory  
41 earthquakes.

**42 Introduction:**

43 Earthquake prediction has been a longstanding goal in seismology (*Rikitake, 1968;*  
44 *Scholz et al., 1973; Dieterich, 1978; Geller, 1997; Hough, 2016*). Part of the difficulty is that  
45 without advanced knowledge of an impending earthquake's location, one cannot focus efforts to  
46 search for so called precursors –temporal changes in rock (or other) properties prior to failure.  
47 However, precursory variations in seismic velocity and amplitude anomalies have been observed  
48 in some cases (*Whitcomb et al., 1973; Crampin et al., 1984; Niu et al., 2008; Malagnini et al.,*  
49 *2019*) and lab work suggests that they might occur for the full spectrum of earthquake failure  
50 modes, from slow slip to elastodynamic earthquakes (*Main and Meredith, 1989; Sammonds et*  
51 *al., 1992; Kaproth and Marone, 2013; Scuderi et al., 2016*). Precursory amplitude variations,  
52 likely related to preslip, have also been observed in limited experiments on sheared rock  
53 discontinuities (*Chen et al., 1993; Hedayat et al., 2014, 2018*). Moreover, recent experimental  
54 studies have used premonitory acoustic emission (AE) signals to predict lab earthquake failure  
55 times (*Rouet-Leduc et al., 2017; Hulbert et al., 2019*). Here, we address the physical  
56 mechanisms responsible for precursors to laboratory earthquakes and focus in particular on the  
57 evolution of fault zone elastic properties as imaged by transmitted wave amplitudes.

58 Active and passive seismic monitoring techniques have proved promising particularly in  
59 the realm of reservoir monitoring (*Lumley et al., 2001; Zhu et al., 2019*) and in field and  
60 laboratory studies of fault frictional state, coseismic energy release and postseismic healing  
61 (*Yoshioka and Iwasa, 2006; Brenguier et al., 2008; Nagata et al., 2008; Latour et al., 2013;*  
62 *Aichele et al., 2018; Shreedharan et al., 2019*). The use of acoustic amplitude (or transmissivity;  
63 see Methods) is particularly appealing here since it has been demonstrated from theory and  
64 experiments (*Kendall and Tabor, 1971; Pyrak-Nolte et al., 1990; Nagata et al., 2008, Saltiel et*

65 *al.*, 2017; Shreedharan *et al.*, 2019) that transmissivity across frictional interfaces is related to  
66 the stiffness and size of asperity contact junctions participating in shear. Specifically, acoustic  
67 transmissivity scales with fault normal stress and healing time and inversely with slip rate during  
68 steady-state shear on experimental faults (Ryan *et al.*, 2018; Shreedharan *et al.*, 2019). These  
69 scaling relationships arise naturally as a result of the relationship between acoustic transmissivity  
70 and asperity stiffness. Therefore, studying p-wave amplitudes enables us to directly study the  
71 micro-scale physics that control the temporal variations in precursors to laboratory earthquakes.  
72 However, whether resolvable precursory signals in transmissivity can be used to monitor the  
73 seismogenic state of tectonic faults remains unclear, although theoretical considerations dictate  
74 that it should be feasible (Kame *et al.*, 2014).

75         Here, we study elastic waves propagating through frictional interfaces during the full  
76 laboratory seismic cycle of loading and failure. We observe preseismic variations in acoustic  
77 transmissivity linked to preslip, and demonstrate that these precursors vary systematically with  
78 fault slip rate and earthquake magnitude. Our results allow us to map transmissivity and asperity  
79 size, and indicate that precursors are a likely outcome of contact area reduction arising from  
80 increasing local fault slip rate during a preparatory phase prior to failure.

81

## 82 **Methods:**

### 83 *Mechanical Data Acquisition*

84         Our experiments were carried out on the biaxial shear apparatus in a double direct-shear  
85 (DDS) configuration in the Penn State Rock Mechanics laboratory. The apparatus was used to  
86 apply normal and shear loads in the horizontal and vertical directions using two hydraulic  
87 pistons. Mechanical data included output from strain gauge load cells and direct current

88 differential transformers (DCDTs) to measure normal and shear loads and displacements,  
89 respectively. The strain gauge load cells, accurate to  $\pm 5$  N, were calibrated with a Morehouse  
90 proving ring. The DCDTs were calibrated using a Vernier height gauge and provide  
91 displacement resolution of  $\pm 0.1$   $\mu\text{m}$ . The DCDTs were mounted on the horizontal and vertical  
92 pistons (inset to Fig 1a) for far-field normal and shear displacement measurements. In addition,  
93 we attached a DCDT to the central shearing block and referenced it to the base of the DDS  
94 configuration to measure true fault slip. Experiments were fully servo-controlled with constant  
95 normal stress and constant shear rate (far-field plate rate) boundary conditions, derived from load  
96 and displacement feedback, respectively.

97         We sheared rough surfaces of Westerly granite that were coated with thin layers of quartz  
98 powder (99.5%  $\text{SiO}_2$ , U.S. Silica product Min-U-Sil 40 with median grain size of 10.5  $\mu\text{m}$ ) to  
99 simulate frictional wear material and fault gouge. Gouge layers weighed  $\sim 0.25$  g and were  $\sim 250$ -  
100  $\mu\text{m}$  thick prior to the application of normal load. The granite surfaces were roughened with #60  
101 grit (RMS roughness  $\sim 20$   $\mu\text{m}$ ). During shear in our experiments, the gouge layers were  
102 comparable in thickness to the maximum surface roughness, resulting in direct interaction  
103 between the fault surfaces and additional wear (Figure S1).

104         Our sample configuration used a nominal contact area of  $5 \times 5$   $\text{cm}^2$ . In the DDS  
105 configuration, the normal stress is applied to hold the three-block configuration together and the  
106 longer central block is sheared between the stationary side blocks. All experiments were  
107 conducted at room temperature and a relative humidity of 100% to ensure reproducibility.  
108 Mechanical data were acquired using a 24-bit  $\pm 10$  V analog-to-digital converter at 10 kHz and  
109 averaged in real-time to 1000 Hz prior to saving.

110 All experiments were performed at a normal stress of 10 MPa and a far-field shear rate of  
 111 11  $\mu\text{m/s}$ . In contrast to previous experimental works (e.g. *Leeman et al., 2016; Scuderi et al.,*  
 112 *2016; Hulbert et al., 2019*) where the continuum of slip modes, from slow to fast frictional stick-  
 113 slips, were generated by varying the normal stress on the sample, we generated the spectrum of  
 114 failure modes by varying the machine loading stiffness using acrylic springs in series with the  
 115 shear loading piston. This approach eliminates the possibility that differences in normal stress  
 116 and in turn frictional contact area and ultrasonic amplitudes (*Shreedharan et al., 2019*) caused  
 117 the effects we observe.

118 Within the framework of frictional slip stability (*Gu et al., 1984*), the transition from  
 119 stable sliding to unstable stick-slip is a consequence of the interactions between the loading  
 120 stiffness,  $k$ , and the rate of fault weakening with slip, which is given by the critical stiffness,  $k_c$ :

$$k < k_c = \frac{\sigma_{eff}(b - a)}{D_c}$$

121 Here,  $\sigma_{eff}$  is the effective normal stress imposed on the sample,  $a$  and  $b$  are rate-state  
 122 friction constants and  $D_c$  is a characteristic slip distance. We vary the ratio of  $k/k_c$  to generate the  
 123 full spectrum of slow and fast stick-slips (*Leeman et al., 2016*) by varying the nominal contact  
 124 area of an acrylic spring in series with the loading column (Inset to Figure 1a; Figure 1b). For  
 125 each experiment, the lab fault was sheared for 35 mm and shear unload-reload cycles were  
 126 performed at  $\sim 2$  mm and  $\sim 4$  mm to measure the effective loading stiffness (*Shreedharan et al.,*  
 127 *2019*) and to accelerate shear localization (*Frye and Marone, 2002*).

128

### 129 *Ultrasonic Acoustic Measurements*

130 Active ultrasonic measurements were performed using broadband ( $\sim 0.02 - 2$  MHz) lead-  
 131 zirconate (PZT) p-polarized ultrasonic transducers (Boston Piezo-Optics Inc. PZT-5A 0.5”

132 compression crystals). The PZT transducers were embedded in steel plates in series with and  
133 coupled to the the DDS block configuration using molasses. Ultrasonic half-sinusoidal pulses  
134 with a frequency of 500 kHz were transmitted through the frictional interfaces at a rate of 1000  
135 pulses per second. Each received waveform was sampled by a Verasonics high-speed digitizer at  
136 25 MHz for  $\sim 80 \mu\text{s}$ , corresponding to a trace length of 2048 samples (Inset to Figure 1a). In this  
137 study, we use the largest peak-to-peak amplitude within the first 5  $\mu\text{s}$  for ultrasonic data analyses,  
138 as highlighted in Figure 1a (yellow waveform). This wavelet represents the transducer response  
139 to the first arrival rather than the p-wave coda used by previous studies (eg. *Scuderi et al., 2016*;  
140 *Tinti et al., 2016*; *Singh et al., 2019*) which represents accumulated effects of multiple reflections  
141 through frictional interfaces and the bulk.

142 The raw amplitudes are then converted to transmissivity values, following previous  
143 works (*Nagata et al., 2008*; *Kilgore et al., 2017*). Here, Transmissivity,  $|T|$ , is the ratio of the  
144 amplitude through the DDS configuration to the amplitude through an intact block having the  
145 same length dimension. This ensures that the reported values are free from bulk deformation  
146 effects. Because each ultrasonic pulse passes through two frictional interfaces, the transmissivity  
147 reported here is the square root of the raw transmissivity (*Nagata et al., 2008*; *Shreedharan et*  
148 *al., 2019*).

149

## 150 **Results:**

151 We sheared rough surfaces of Westerly granite decorated with a thin coating of quartz  
152 powder to simulate earthquake fault zones. We monitored stresses, fault displacements, and fault  
153 slip rate (Fig 1) while conducting continuous ultrasonic monitoring for a range of fault slip  
154 modes, slip velocities and stress drops (refer to Supplementary Table S1 for boundary

155 conditions). Our experiments were designed to maintain constant frictional contact area and  
156 normal stress, which have a non-trivial effect on transmissivity (*Shreedharan et al., 2019*).  
157 Supplementary Figure S2 shows the effect of varying spring cross-sectional area on stiffness.  
158 Generally, the loading stiffness increases linearly with cross-sectional area. We observe a  
159 transition from stable sliding to quasi-dynamic and subsequently repetitive stick-slips after  
160 approximately 8-10 mm of shear (Fig. 1a). Our experiments show consistent results including,  
161 for some conditions, period-doubling (Inset to Fig. 1a) behavior with alternating slow and fast  
162 stick-slips, likely due to interactions between the gouge layers and the rough frictional interface  
163 of the granite. This observation is consistent with period-doubling observed in numerical  
164 simulations (*Gu et al., 1984*), in friction experiments when the loading stiffness is close to the  
165 critical weakening rate (*Leeman et al., 2016; Scuderi et al. 2016*) and in nature, along the San  
166 Andreas fault (*Veedu and Barbot, 2016*).

167 We report measurements of stress drop, peak slip velocity, slip duration and the effective  
168 machine loading stiffness for each stick-slip event (Fig. 1). Following *Leeman et al. (2016,*  
169 *2018)*, we classify slow laboratory earthquakes as the instabilities without audible co-seismic  
170 energy radiation. In our experiments, slow earthquakes have stress drops of 0.3 MPa or less,  
171 maximum peak slip velocities of 300  $\mu\text{m/s}$  and co-seismic durations  $> 0.5$  s. Consistent with  
172 previous observations (*Ide et al., 2007; Peng and Gomberg, 2010; Leeman et al., 2016; Scuderi*  
173 *et al., 2016*), slow-slip events have consistently smaller stress drops than dynamic stick-slip  
174 instabilities. Additionally, stress drops are negatively correlated with loading stiffness, with the  
175 more compliant system producing larger, more audible instabilities (Fig. 1b). Earthquake stress  
176 drops also increase with increasing peak co-seismic slip velocities (Fig. 1c) and decrease with  
177 higher co-seismic slip durations (Fig. 1d).

178 A representative set of stick-slips and their associated mechanical and ultrasonic  
179 attributes are shown in Fig. 2, with Fig. 2a and Fig. 2b expressing the instabilities as functions of  
180 the imposed far-field shear displacement rate and fault slip rate respectively. We measure the  
181 coefficient of friction (hereafter referred to as friction) as the ratio of fault zone shear and normal  
182 stresses. Within the period-doubling space, slow instabilities have peak slip velocities of  $\sim 100$   
183  $\mu\text{m/s}$  and fast elastodynamic events have peak slip rates of  $\sim 1$  mm/s, representing an order of  
184 magnitude increase in peak slip rate (Fig. 2a). Observations of fault normal displacement  
185 indicate that the faults undergo dilation during the interseismic period (linear-elastic loading  
186 phase), begin to compact prior to failure and undergo rapid compaction during the primary stress  
187 drop as the fault slip rate reduces to near zero and the fault locks up (Fig. 2b). This indicates that  
188 compaction and reduced post-seismic slip rate could work in concert to enhance fault healing, by  
189 increasing the number and size of frictional contact junctions (*Yasuhara et al., 2005*). Ultrasonic  
190 amplitude, expressed as transmissivity, first increases during elastic loading and then decrease  
191 prior to failure for both slow and fast slip events (Fig 2a). Interestingly, the onset of preseismic  
192 transmissivity reduction also marks the onset of inelastic fault creep and an increase in fault slip  
193 rate. That is, the p-wave amplitudes decrease once the fault begins to unlock and inelastic  
194 loading occurs (Fig 2a). Subsequently, the amplitudes reduce to a minimum during the co-  
195 seismic slip phase when the fault reaches its peak slip rate (Fig. 2b).

196

**197 Discussion:**

198 Taken together, the variations in elastic wave amplitudes and fault slip during our  
199 laboratory earthquakes indicate that the precursory variations in amplitudes quantitatively track  
200 fault slip rate (Fig. 3). This observation is consistent with the long-held assertion that preslip and

201 nucleation zone damage could dictate the characteristics of earthquake precursors in nature  
202 (*Dieterich, 1978; Chen et al., 1993; Hedayat et al., 2014; Scholz, 2019; Acosta et al., 2019*).  
203 Broadly, variations in amplitudes observed in our experiments can be classified into two  
204 preseismic stages (Fig. 3a, e). First, the increase in wave amplitude during the linear-elastic  
205 loading phase of the interseismic period, which follows fault slip deceleration and subsequent  
206 lock-up after failure (Fig. 3a, e). During the linear-elastic loading phase, the amplitude increases  
207 logarithmically with time (Fig. 3b, f), consistent with observations of fault healing in friction  
208 experiments (*Dieterich, 1972; Ryan et al., 2018; Shreedharan et al., 2019*) and in nature  
209 (*Marone, 1998a,b; Brenguier et al., 2008*). We interpret this increase in transmissivity as an  
210 increase in the specific stiffness (see supplementary Figure S3) and strength of microscopic  
211 contact junctions that make up the granular interface, either via an increase in the number or size  
212 (or both) of asperities during the ‘healing’ phase (*Li et al., 2011; Shreedharan et al., 2019*).

213 The second stage is marked by the onset of inelastic fault creep prior to failure for fast  
214 (Fig. 3a) and slow slip events (Fig. 3e) and begins when amplitude has reached a peak value.  
215 This systematic transition from first to second stage makes transmissivity a reliable precursor to  
216 failure. Transmissivity reduces continuously during the second stage until the fault reaches its  
217 minimum shear stress during co-seismic failure, with the reduction being linear in log-time (Fig.  
218 3c, g).

219 During co-seismic fault slip, the transmitted wave amplitudes attain a minimum  
220 coincident with peak fault slip rate. The maxima and minima attained by fault slip and  
221 amplitudes respectively also correspond to the peak frictional unloading rate. It is interesting to  
222 note that we observe no break in slope in the amplitude-time variation during the transition from  
223 pre- to co-seismic slip (Fig. 3c and Fig. 3e). This indicates that the contact-scale mechanics

224 controlling slip behavior may be similar for both pre- and co-seismic slip. The two-stage nature  
225 of the wave amplitude precursor is consistent with previous works that documented an elastic  
226 wave velocity precursor that was controlled by fault zone preslip (*Kaproth and Marone, 2013*;  
227 *Scuderi et al., 2016*). When expressed as a function of logarithmic slip rate, the elastic amplitude  
228 varies systematically (Fig. 3d, h). Both the increase and decrease in amplitude during the  
229 interseismic period follow the same slope. Preseismic amplitude variations documented in our  
230 experiments could be indicative of cascading, predictable failure (*Hulbert et al., 2019*). Thus, our  
231 results suggest that continuous seismic monitoring may be used in natural settings to gather  
232 insight into imminent fault failure. However, we note that extrapolating our results to field scales  
233 may not be straightforward. In particular, preslip on natural faults is often small and may not  
234 always be resolvable (eg. *Amoruso and Crescentini, 2009*). Additionally, at low strain rates  
235 approaching those experienced by natural faults, acoustic emission foreshock precursors have  
236 been observed to become temporally shorter, occurring closer to failure (*Ojala et al., 2004*).

237 Figure 4 shows the relationship between preseismic slip, co-seismic stress drops and  
238 precursory amplitude reduction prior to failure. Preseismic slip is calculated here as the total slip  
239 undergone, as measured by the across fault displacement transducer (Fig. 1a), between the  
240 interseismic minimum shear stress and peak shear stress just before failure. Our results indicate a  
241 robust relationship between elastic amplitudes and precursory slip (Fig. 4). These observations  
242 are consistent with previous AE studies that have suggested that microscopic slip is related to the  
243 increase in AE activity prior to stick-slips and with recent observations of precursory damage  
244 prior to failure (*Niu et al., 2008*; *Johnson et al., 2013*).

245 Preslip has been shown to vary with both effective normal stress as well as loading rate  
246 (*Scuderi et al., 2015*; *Leeman et al., 2018*; *Acosta et al., 2019*). However, the effect of fault zone

247 stiffness alone on preseismic slip is not well documented. Our observations of stiffness show that  
248 preslip varies inversely with stress drop magnitude (Fig. 4a) for the range of stiffnesses explored  
249 in this study. In other words, faults experiencing higher preslip release some of the accumulated  
250 strain energy via pre-seismic sliding resulting in a lower co-seismic stress drop magnitude  
251 (*Cattania and Segall, 2019*). This is consistent with the theory of time-dependent healing  
252 (*Dieterich, 1978; Marone, 1998b*) within the framework of rate-and-state friction, where higher  
253 healing is associated with an increase in subsequent seismic magnitude via an increase in real  
254 area of contact at asperity junctions. Specifically, as we increase fault zone stiffness, we observe  
255 a transitioning to stable sliding, representing infinite preslip.

256 Simultaneously, we calculate the reduction in preseismic amplitudes as the percent  
257 reduction from peak amplitude during elastic loading ( $A_{\max}$ ) to the amplitude at peak friction  
258 prior to failure ( $A_{\cos}$ ), referenced against the peak amplitude (Fig 3; Fig. 4b). We observe that the  
259 precursory amplitude variations are systematically higher when the fault experiences little to no  
260 preseismic slip (e.g. largest slip events). Conversely, the smallest precursory amplitude  
261 signatures are associated with the highest preseismic slip and smaller magnitude slip events. This  
262 indicates that the fault locks up more (i.e., experiences a lower interseismic minimum in slip  
263 rate) preceding ruptures with large stress drop. This allows for a higher magnitude of healing and  
264 longer healing times preceding larger co-seismic stress drops. Thus, while the onset of the  
265 precursory amplitude reduction is related to the temporal onset of preslip, the size of the  
266 amplitude precursor is intimately related to the maximum slip rate excursion experienced by the  
267 fault. This is apparent in Fig. 3a and Fig. 3d when the interseismic amplitude increases rapidly  
268 for  $\sim 2$  s for the fast rupture, whereas it increases more gradually for  $\sim 0.5$  s when the strain  
269 accumulation culminates in a slow earthquake (Fig. 3e). Finally, our observations of the

270 precursory amplitude variation indicate that the onset of the amplitude precursor occurs earlier in  
271 the seismic cycle when the fault undergoes less macroscopic preslip and the onset is delayed as  
272 the fault undergoes more preslip (Fig. 4c). The fault achieves lower slip rates earlier in the  
273 interseismic period preceding larger instabilities, and elastic wave amplitudes are related to the  
274 logarithm of the fault slip rate. Hence, the onset of small microslip precursors produces large,  
275 resolvable precursory amplitude signals earlier in the interseismic period preceding large  
276 laboratory earthquakes.

277 We cast the temporal onset of transmissivities in the context of natural earthquakes by  
278 converting coseismic slip into seismic moment (*Acosta et al. 2019*). We assume a shear modulus  
279 of 3 GPa for quartz gouge (*Kenigsberg et al., 2019*) and that the entire fault area ( $25 \text{ cm}^2$ )  
280 ruptures which is reasonable when the fault patch is smaller than a critical nucleation length  
281 (*McLaskey and Lockner, 2014*). Our results (Figure 4d) fall remarkably close to the scaling  
282 between onset of precursors and eventual earthquake size reported by Scholz et al. (1973). This  
283 demonstrates that similar microphysical processes could operate in concert to produce precursors  
284 over multiple scales.

285

## 286 **Conclusions and Future Directions**

287 We report on the evolution of fault zone elastic properties throughout the laboratory  
288 seismic cycle. The transmitted wave amplitude robustly tracks precursory fault slip prior to both  
289 slow and fast laboratory earthquakes. Our observations indicate that elastic wave amplitudes are  
290 robust, scalable precursors to failure that are consistent with and higher resolution than elastic  
291 wave velocity precursors. Our data suggest that time-lapse active seismic monitoring of faults in  
292 nature could provide critical information pertinent to preslip, foreshocks and imminent failure.

293 The utility of active seismic monitoring of wave amplitude has been consistently demonstrated in  
294 theoretical studies (*Kame et al., 2014*) and in limited field-based surveys such as those related to  
295 CO<sub>2</sub> injection and storage (*Arts et al., 2004; Zhu et al., 2019*). Future research should focus on  
296 applying active seismic techniques to monitor fault zones for hazard quantification and  
297 mitigation (e.g., *Niu et al., 2008*). Finally, our results demonstrate the similarity between the  
298 microphysical mechanisms operating before slow and fast earthquakes, which has important  
299 implications to further our understanding of the mechanics of slow slip and the feedbacks  
300 between the observed spectrum of tectonic slip modes.

301

302 **Acknowledgements:**

303 We thank Ake Fagereng, Ian Main and an anonymous reviewer for comments. Technical  
304 assistance from laboratory manager Steve Swavely is gratefully acknowledged. This study was  
305 supported by NSF-EAR1520760 , DOE Office of Basic Energy Science contract DE-  
306 SC0017585, and a Schlanger Fellowship to S.S. Data are available from the PSU Scholarsphere  
307 repository (<https://doi.org/10.26207/12jy-rw97>) or by contacting the corresponding author.

308

309

310 **Figures:**

311 **Figure 1.** The spectrum of fault slip modes generated by modifying the acrylic spring cross-  
312 sectional area (see inset). (a) Friction-displacement for a representative experiment shows the  
313 transition from stable sliding to stick-slip behavior after approximately 7 mm shear. Two unload-  
314 reload cycles are performed at ~2 mm and ~4 mm shear displacement. Left (bottom) inset shows  
315 a schematic of the double-direct shear setup with ultrasonic monitoring and slip sensor. Middle  
316 inset shows a typical ultrasonic pulse passing through the frictional interfaces with the analyzed  
317 peak-to-peak amplitudes highlighted in yellow. Right inset shows a sequence of period-doubling  
318 stick-slips and associated fault slip. (b) Static stress-drops expressed as a function of elastic  
319 loading stiffness shows an inverse trend. Colors denote different spring sizes shown in (a). Black  
320 dots represent mean values and error bars represent 1 standard deviation. (c) Peak slip velocity  
321 increases with higher stress-drops and (d) higher stress-drops are associated with lower co-  
322 seismic slip durations. In b-d, the grey region denotes silent slow laboratory earthquakes and  
323 stick-slip datasets correspond to events in the range of 18 – 21 mm.

324

325

326 **Figure 2.** Variation of fault zone dilation, slip rate and elastic amplitudes,  $|T|$ , during stick-slips.  
327 Grey boxes denote the co-seismic slip phase of a slow and fast slip event. (a) Friction drops, fault  
328 zone dilation, fault slip rate and elastic amplitudes are shown as functions of far-field imposed  
329 loading rate. Slow stick-slips are characterized by smaller stress drops than fast stick-slips for a  
330 given set of boundary conditions. During the co-seismic slip stage, the fault zone compacts, slip  
331 rate accelerates and elastic amplitudes attain a minimum value. Note that slow-slip events are  
332 also characterized by smaller peak slip velocities than faster ruptures. The preseismic reduction  
333 in amplitudes occurs during the interseismic strain accumulation phase of the stick-slip event. (b)  
334 The fault zone attributes in (a) expressed as functions of measured fault slip. Elastic amplitudes  
335 and fault zone dilation reach their respective minimum values during the maximum strain release  
336 rate portion of the co-seismic stress drop. Simultaneously, the fault slip rate reaches its maximum  
337 value.  
338  
339

340

341 **Figure 3.** The relationship between precursory amplitude variation and fault slip rate for slow  
342 (panels a-d) and fast laboratory earthquakes (panels e-h). (a) and (e) show friction (black), slip  
343 rate (green) and p-wave amplitude (purple) evolution for a representative fast and slow  
344 laboratory earthquake respectively. Note the short slip duration and large friction drop for the  
345 fast slip versus the longer transient slip duration for the slow slip. Dashed lines show the loading  
346 stiffness of the stick-slip instability. Elastic amplitudes begin to reduce at the onset of inelastic  
347 loading and continue to decrease throughout the co-seismic slip phase. (b) and (f) show the  
348 increasing limb of preseismic amplitudes expressed versus time since previous event on a  
349 logarithmic scale. The log-linear relationship of the increasing limb between amplitude and time  
350 demonstrates fault healing via contact area increase. while (c) and (g) show the reduction in  
351 amplitudes from interseismic peak to co-seismic minimum, expressed as a function of time until  
352 fault failure. (d) and (h) elastic amplitudes as a function of slip rate and colored with reference to  
353 time to failure of the next slip event. Elastic amplitudes vary log-linearly with fault slip rate.  
354 Amplitudes reduce at the onset of preseismic fault slip (see a) and continue to reduce at the same  
355 rate until they attain a minimum value during the co-seismic slip stage.

356

357

358

359 **Figure 4.** Relationship between preslip, precursors and earthquake size. (a) Static stress-drop and  
360 preseismic slip are inversely related to each other for a given normal stress and imposed loading  
361 rate (b) Preseismic amplitude reduction scales inversely with preseismic slip, and thus, is directly  
362 correlated to the magnitude of the slip event. (c) Preseismic amplitudes reduce earlier in the  
363 interseismic period for slip events with smaller amounts of preslip and larger stress drops. (d)  
364 Onset of precursors increases as a function of magnitude of subsequent earthquakes showing  
365 consistency across several scales.

366

367

368 **References:**

- 369 Acosta, M., Passelegue, F. X., Schubnel, A., Madariaga, R., & Violay, M. (2019). Can  
370 precursory moment release scale with earthquake magnitude? A view from the  
371 laboratory. *Geophysical Research Letters*.
- 372 Aichele, J., Catheline, S., Roux, P., Latour, S., & Voisin, C. (2018, July). Ultrafast ultrasound  
373 captures dynamic rupture behavior. In *Proceedings of Meetings on Acoustics 211SNA* (Vol.  
374 34, No. 1, p. 045044). ASA.
- 375 Amoruso, A., & Crescentini, L. (2009). Slow diffusive fault slip propagation following the 6  
376 April 2009 L'Aquila earthquake, Italy. *Geophysical Research Letters*, 36(24).
- 377 Arts, R., Eiken, O., Chadwick, A., Zweigel, P., Van der Meer, L., & Zinszner, B. (2004).  
378 Monitoring of CO<sub>2</sub> injected at Sleipner using time-lapse seismic data. *Energy*, 29(9-10),  
379 1383-1392.
- 380 Brenguier, F., Campillo, M., Hadziioannou, C., Shapiro, N. M., Nadeau, R. M., & Larose, E.  
381 (2008). Postseismic relaxation along the San Andreas fault at Parkfield from continuous  
382 seismological observations. *science*, 321(5895), 1478-1481.
- 383 Cattania, C., & Segall, P. (2019). Crack Models of Repeating Earthquakes Predict Observed  
384 Moment-Recurrence Scaling. *Journal of Geophysical Research: Solid Earth*, 124(1), 476-503.
- 385 Chen, W. Y., Lovell, C. W., Haley, G. M., & Pyrak-Nolte, L. J. (1993, December). Variation of  
386 shear-wave amplitude during frictional sliding. In *International journal of rock mechanics  
387 and mining sciences & geomechanics abstracts* (Vol. 30, No. 7, pp. 779-784). Pergamon.
- 388 Crampin, S., Evans, R., & Atkinson, B. K. (1984). Earthquake prediction: a new physical  
389 basis. *Geophysical Journal International*, 76(1), 147-156.

- 390 Dieterich, J. H. (1972). Time-dependent friction in rocks. *Journal of Geophysical*  
391 *Research*, 77(20), 3690-3697.
- 392 Dieterich, J. H. (1978). Preseismic fault slip and earthquake prediction. *Journal of Geophysical*  
393 *Research: Solid Earth*, 83(B8), 3940-3948.
- 394 Frye, K. M., & Marone, C. (2002). The effect of particle dimensionality on granular friction in  
395 laboratory shear zones. *Geophysical Research Letters*, 29(19), 22-1.
- 396 Geller, R. J. (1997). Earthquake prediction: a critical review. *Geophysical Journal*  
397 *International*, 131(3), 425-450.
- 398 Gu, J. C., Rice, J. R., Ruina, A. L., & Simon, T. T. (1984). Slip motion and stability of a single  
399 degree of freedom elastic system with rate and state dependent friction. *Journal of the*  
400 *Mechanics and Physics of Solids*, 32(3), 167-196.
- 401 Hedayat, A., Pyrak-Nolte, L. J., & Bobet, A. (2014). Precursors to the shear failure of rock  
402 discontinuities. *Geophysical Research Letters*, 41(15), 5467-5475.
- 403 Hedayat, A., Haeri, H., Hinton, J., Masoumi, H., & Spagnoli, G. (2018). Geophysical Signatures  
404 of Shear-Induced Damage and Frictional Processes on Rock Joints. *Journal of Geophysical*  
405 *Research: Solid Earth*, 123(2), 1143-1160.
- 406 Hough, S. E. (2016). *Predicting the unpredictable: the tumultuous science of earthquake*  
407 *prediction*. Princeton University Press.
- 408 Hulbert, C., Rouet-Leduc, B., Johnson, P. A., Ren, C. X., Rivière, J., Bolton, D. C., & Marone,  
409 C. (2019). Similarity of fast and slow earthquakes illuminated by machine learning. *Nature*  
410 *Geoscience*, 12(1), 69.
- 411 Ide, S., Beroza, G. C., Shelly, D. R., & Uchide, T. (2007). A scaling law for slow  
412 earthquakes. *Nature*, 447(7140), 76.

- 413 Johnson, P. A., Ferdowsi, B., Kaproth, B. M., Scuderi, M., Griffa, M., Carmeliet, J., Guyer, R.  
414 A., Le Bas, P-Y., Trugman, D. T., & Marone, C. (2013). Acoustic emission and microslip  
415 precursors to stick-slip failure in sheared granular material. *Geophysical Research*  
416 *Letters*, 40(21), 5627-5631.
- 417 Kame, N., Nagata, K., Nakatani, M., & Kusakabe, T. (2014). Feasibility of acoustic monitoring  
418 of strength drop precursory to earthquake occurrence. *Earth, Planets and Space*, 66(1), 41.
- 419 Kaproth, B. M., & Marone, C. (2013). Slow earthquakes, preseismic velocity changes, and the  
420 origin of slow frictional stick-slip. *Science*, 341(6151), 1229-1232.
- 421 Kendall, K., & Tabor, D. (1971). An ultrasonic study of the area of contact between stationary  
422 and sliding surfaces. *Proceedings of the Royal Society of London. A. Mathematical and*  
423 *Physical Sciences*, 323(1554), 321-340.
- 424 Kenigsberg, A. R., Rivière, J., Marone, C., & Saffer, D. M. (2019). The effects of shear strain,  
425 fabric, and porosity evolution on elastic and mechanical properties of clay-rich fault  
426 gouge. *Journal of Geophysical Research: Solid Earth*, 124.  
427 <https://doi.org/10.1029/2019JB017944>
- 428 Kilgore, B., Beeler, N. M., Lozos, J., & Oglesby, D. (2017). Rock friction under variable normal  
429 stress. *Journal of Geophysical Research: Solid Earth*, 122(9), 7042-7075.
- 430 Latour, S., Voisin, C., Renard, F., Larose, E., Catheline, S., & Campillo, M. (2013). Effect of  
431 fault heterogeneity on rupture dynamics: An experimental approach using ultrafast ultrasonic  
432 imaging. *Journal of Geophysical Research: Solid Earth*, 118(11), 5888-5902.
- 433 Leeman, J. R., Saffer, D. M., Scuderi, M. M., & Marone, C. (2016). Laboratory observations of  
434 slow earthquakes and the spectrum of tectonic fault slip modes. *Nature communications*, 7,  
435 11104.

- 436 Leeman, J. R., Marone, C., & Saffer, D. M. (2018). Frictional mechanics of slow  
437 earthquakes. *Journal of Geophysical Research: Solid Earth*, 123(9), 7931-7949.
- 438 Li, Q., Tullis, T. E., Goldsby, D., & Carpick, R. W. (2011). Frictional ageing from interfacial  
439 bonding and the origins of rate and state friction. *Nature*, 480(7376), 233.
- 440 Lumley, D. E. (2001). Time-lapse seismic reservoir monitoring. *Geophysics*, 66(1), 50-53.
- 441 Main, I. G., & Meredith, P. G. (1989). Classification of earthquake precursors from a fracture  
442 mechanics model. *Tectonophysics*, 167(2-4), 273-283.
- 443 Malagnini, L., Dreger, D. S., Bürgmann, R., Munafò, I., & Sebastiani, G. (2019). Modulation of  
444 seismic attenuation at Parkfield, before and after the 2004 M6 earthquake. *Journal of*  
445 *Geophysical Research: Solid Earth*.
- 446 Marone, C. (1998a). Laboratory-derived friction laws and their application to seismic  
447 faulting. *Annual Review of Earth and Planetary Sciences*, 26(1), 643-696.
- 448 Marone, C. (1998b). The effect of loading rate on static friction and the rate of fault healing  
449 during the earthquake cycle. *Nature*, 391(6662), 69.
- 450 McLaskey, G., & Lockner, D. A. (2014). Preslip and cascade processes initiating laboratory stick  
451 slip. *Journal of Geophysical Research: Solid Earth*, 119, 6323–6336.  
452 <https://doi.org/10.1002/2014JB011220>
- 453 Nagata, K., Nakatani, M., & Yoshida, S. (2008). Monitoring frictional strength with acoustic  
454 wave transmission. *Geophysical Research Letters*, 35(6).
- 455 Niu, F., Silver, P. G., Daley, T. M., Cheng, X., & Majer, E. L. (2008). Preseismic velocity  
456 changes observed from active source monitoring at the Parkfield SAFOD drill  
457 site. *Nature*, 454(7201), 204.

- 458 Ojala, I. O., Main, I. G., & Ngwenya, B. T. (2004). Strain rate and temperature dependence of  
459 Omori law scaling constants of AE data: Implications for earthquake foreshock-aftershock  
460 sequences. *Geophysical Research Letters*, *31*(24).
- 461 Peng, Z., & Gomberg, J. (2010). An integrated perspective of the continuum between  
462 earthquakes and slow-slip phenomena. *Nature geoscience*, *3*(9), 599.
- 463 Pyrak-Nolte, L. J., Myer, L. R., & Cook, N. G. (1990). Transmission of seismic waves across  
464 single natural fractures. *Journal of Geophysical Research: Solid Earth*, *95*(B6), 8617-8638.
- 465 Rikitake, T. (1968). Earthquake prediction. *Earth-Science Reviews*, *4*, 245-282.
- 466 Rouet-Leduc, B., Hulbert, C., Lubbers, N., Barros, K., Humphreys, C. J., & Johnson, P. A.  
467 (2017). Machine learning predicts laboratory earthquakes. *Geophysical Research*  
468 *Letters*, *44*(18), 9276-9282.
- 469 Ryan, K. L., Rivière, J., & Marone, C. (2018). The Role of Shear Stress in Fault Healing and  
470 Frictional Aging. *Journal of Geophysical Research: Solid Earth*, *123*(12), 10-479.
- 471 Saltiel, S., Selvadurai, P. A., Bonner, B. P., Glaser, S. D., & Ajo-Franklin, J. B. (2017).  
472 Experimental development of low-frequency shear modulus and attenuation measurements in  
473 mated rock fractures: Shear mechanics due to asperity contact area changes with normal  
474 stress. *Geophysics*, *82*(2), M19-M36.
- 475 Sammonds, P. R., Meredith, P. G., & Main, I. G. (1992). Role of pore fluids in the generation of  
476 seismic precursors to shear fracture. *Nature*, *359*(6392), 228.
- 477 Scholz, C. H., Sykes, L. R., & Aggarwal, Y. P. (1973). Earthquake prediction: a physical  
478 basis. *Science*, *181*(4102), 803-810.
- 479 Scholz, C. H. (2019). *The mechanics of earthquakes and faulting*. Cambridge university press.

- 480 Scuderi, M. M., Marone, C., Tinti, E., Di Stefano, G., & Collettini, C. (2016). Precursory  
481 changes in seismic velocity for the spectrum of earthquake failure modes. *Nature*  
482 *geoscience*, 9(9), 695.
- 483 Shreedharan, S., Rivière, J., Bhattacharya, P., & Marone, C. (2019). Frictional State Evolution  
484 during Normal Stress Perturbations Probed with Ultrasonic Waves. *Journal of Geophysical*  
485 *Research: Solid Earth*.
- 486 Singh, J., Curtis, A., Zhao, Y., Cartwright-Taylor, A., & Main, I. (2019). Coda Wave  
487 Interferometry for Accurate Simultaneous Monitoring of Velocity and Acoustic Source  
488 Locations in Experimental Rock Physics. *Journal of Geophysical Research: Solid Earth*.
- 489 Tinti, E., Scuderi, M. M., Scognamiglio, L., Di Stefano, G., Marone, C., & Collettini, C. (2016).  
490 On the evolution of elastic properties during laboratory stick-slip experiments spanning the  
491 transition from slow slip to dynamic rupture. *Journal of Geophysical Research: Solid*  
492 *Earth*, 121(12), 8569-8594.
- 493 Veedu, D. M., & Barbot, S. (2016). The Parkfield tremors reveal slow and fast ruptures on the  
494 same asperity. *Nature*, 532(7599), 361.
- 495 Whitcomb, J. H., Garmany, J. D., & Anderson, D. L. (1973). Earthquake prediction: Variation of  
496 seismic velocities before the San Francisco earthquake. *Science*, 180(4086), 632-635.
- 497 Yasuhara, H., Marone, C., & Elsworth, D. (2005). Fault zone restrengthening and frictional  
498 healing: The role of pressure solution. *Journal of Geophysical Research: Solid*  
499 *Earth*, 110(B6).
- 500 Yoshioka, N., & Iwasa, K. (2006). A laboratory experiment to monitor the contact state of a fault  
501 by transmission waves. *Tectonophysics*, 413(3-4), 221-238.

502 Zhu, T., Ajo-Franklin, J., Daley, T. M., & Marone, C. (2019). Dynamics of geologic CO<sub>2</sub> storage  
503 and plume motion revealed by seismic coda waves. *Proceedings of the National Academy of*  
504 *Sciences*, *116*(7), 2464-2469.

Figure 1.

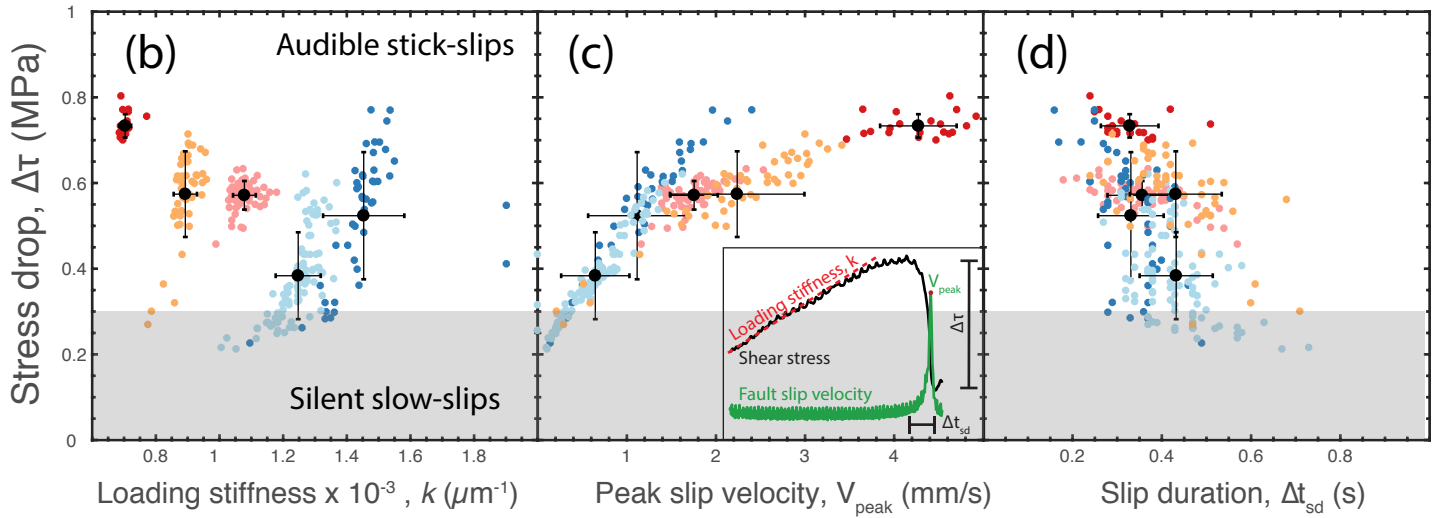
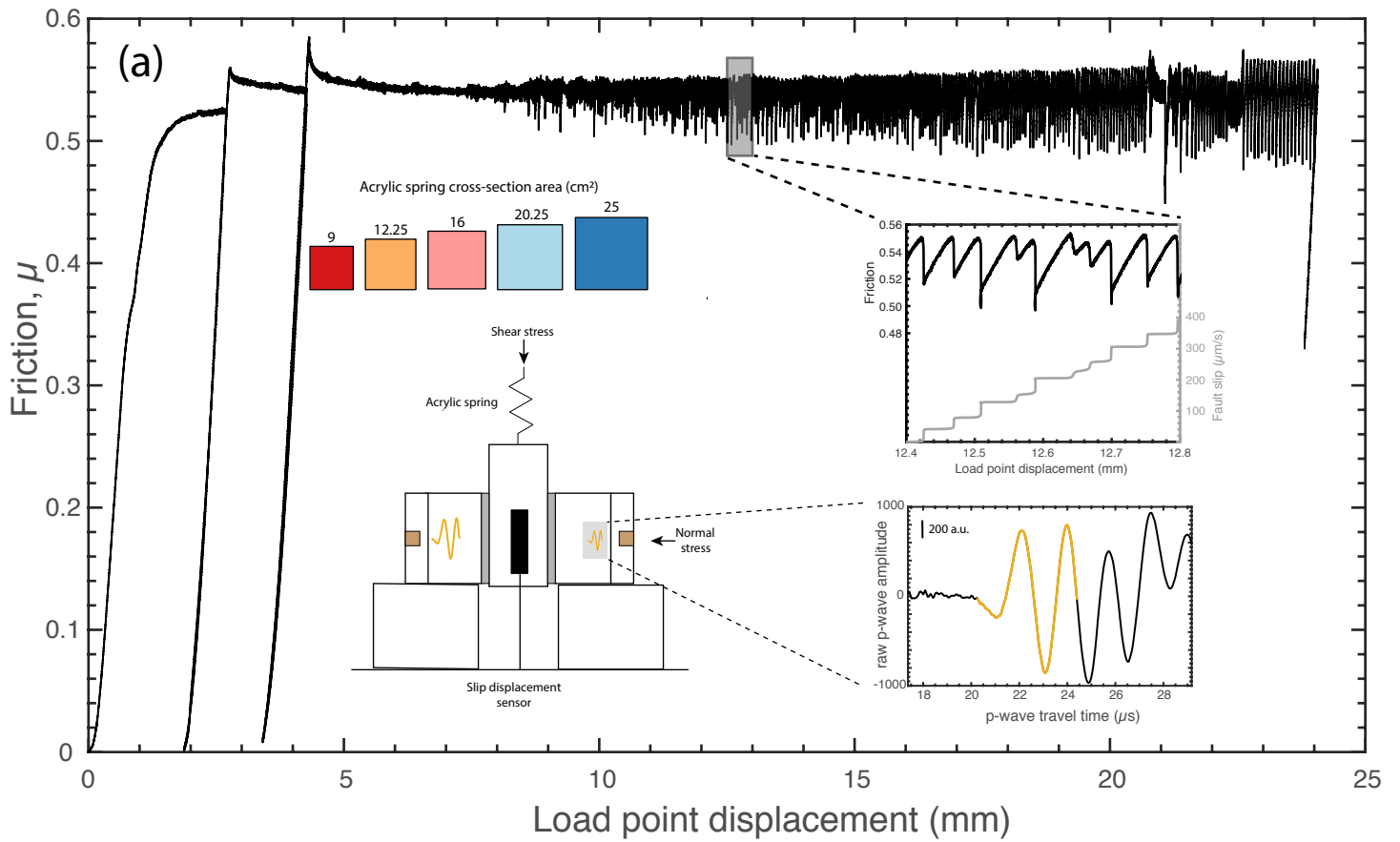


Figure 2.

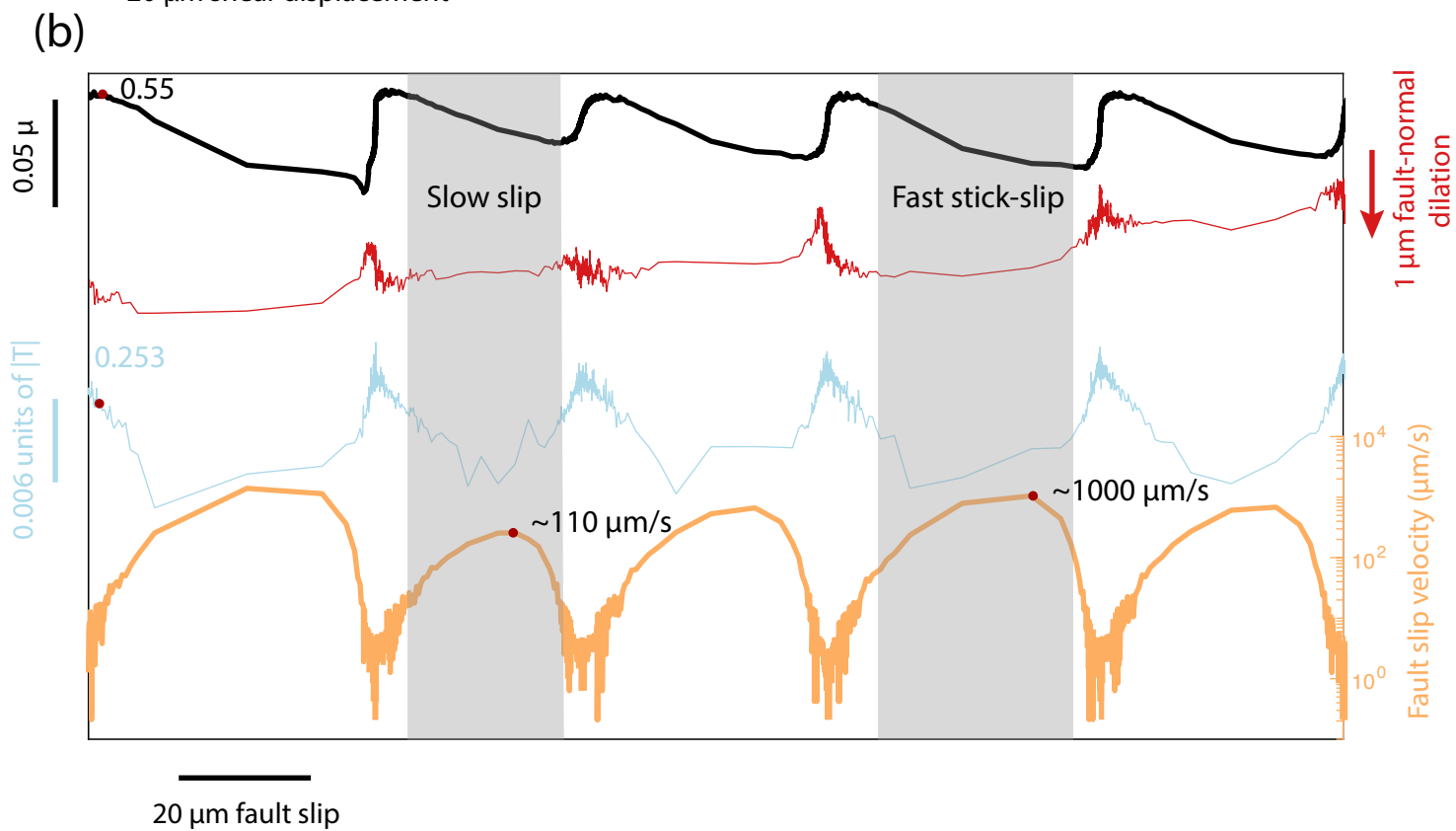
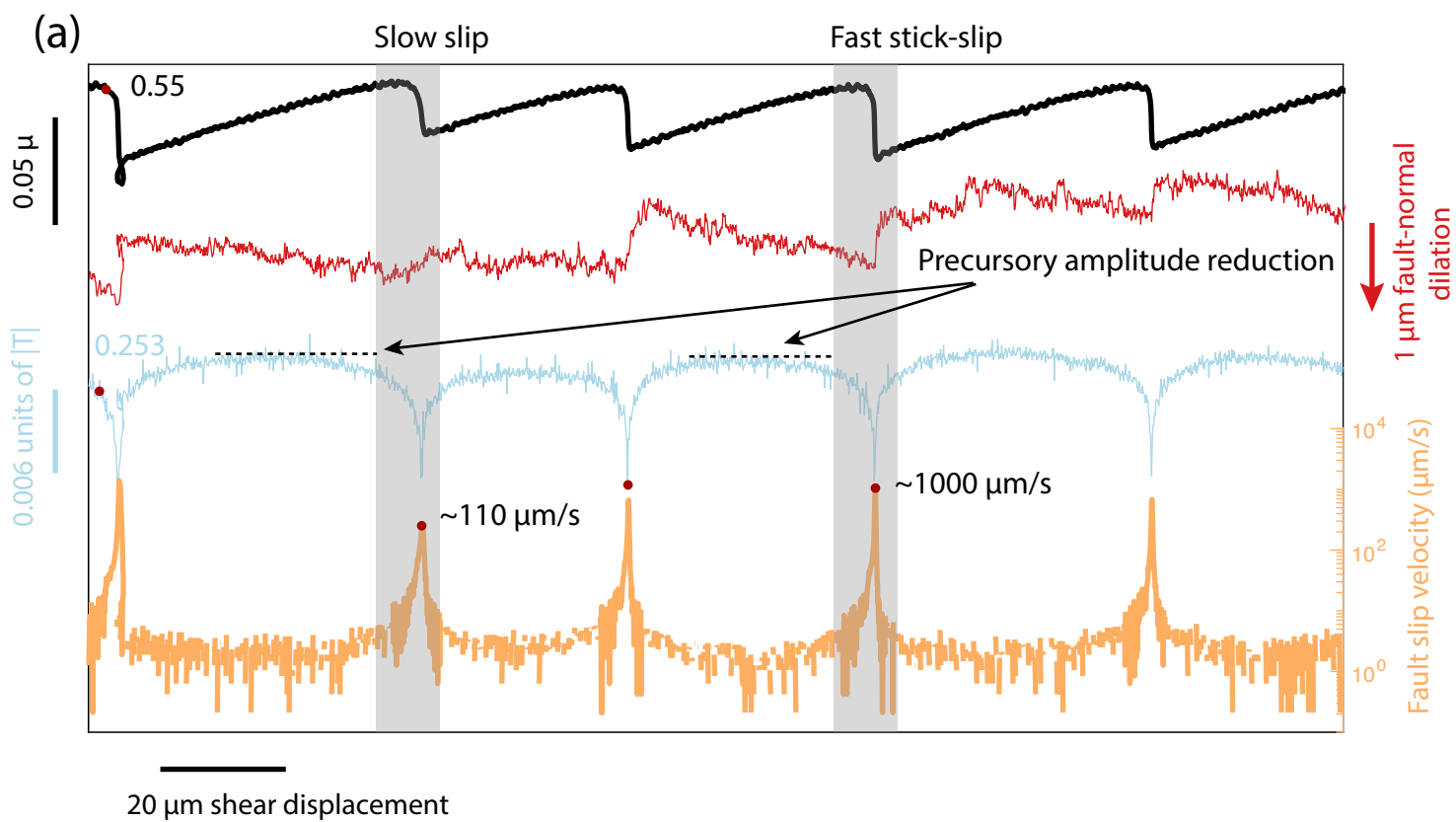
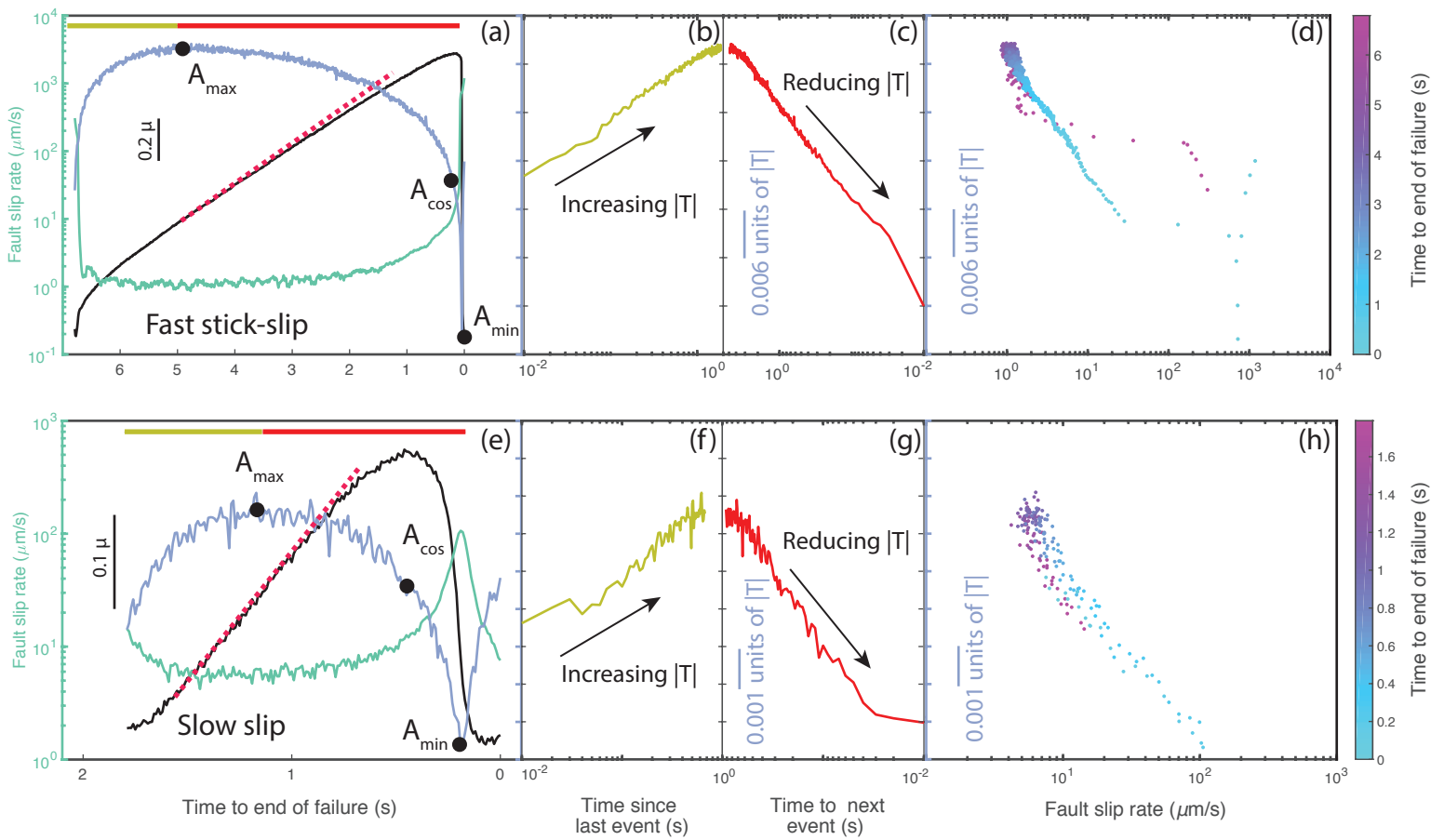


Figure 3.



**Figure 4.**

